IEEE Access
Multidisciplinary | Rapid Review | Open Access Journal

Received August 29, 2019, accepted September 21, 2019, date of publication October 2, 2019, date of current version October 23, 2019.

Digital Object Identifier 10.1109/ACCESS.2019.2945082

Efficient Aerodynamic Shape Optimization of the Hypersonic Lifting Body Based on Free Form Deformation Technique

BIN ZHANG, ZHIWEI FENG, BOTING XU, AND TAO YANG
College of Aerospace Science and Engineering, National University of Defense Technology, Changsha 410073, China

Corresponding author: Zhiwei Feng (fzwnudt@163.com)

This work was supported in part by the National Natural Science Foundation of China under Grant 11772353.

ABSTRACT Aerodynamic shape optimization (ASO) of hypersonic lifting body has become a significant research topic due to its significant performance advantages. As a universal parameterization, the free form deformation (FFD) technique has benefits including geometric independence, random deformation, and mesh synchronization. In this paper, an effective design method to apply the FFD technique in the ASO of a hypersonic lifting body is presented. Some commonly used basis functions are researched in FFD modeling of the windward side of a typical lifting body, including the Bernstein polynomial, the B-spline function, and the non-uniform rational B-spline (NURBS) function. An efficient aerodynamic simulation method combining Euler equations (non-viscous component) and skin friction drag (viscous component based on the compressible turbulence model) is then developed to minimize computational requirements. The accuracy of the proposed method is validated, and a significant decrease in processing time is observed. In addition, a kriging surrogate model combined with infilling sampling expected improvement (EI) criterion is developed to improve optimization efficiency. To obtain a lifting body with high lift-to-drag ratio that satisfies inner loading constraint, a baseline is optimized by manipulating its shape using the NURBS-based FFD technique. The results show that the optimal shape displays outstanding aerodynamic performance, and the effective design method can provide practical support for ASO of the hypersonic lifting body.

INDEX TERMS Aerodynamic shape optimization, hypersonic lifting body, free form deformation, surrogate-based optimization.

I. INTRODUCTION

A hypersonic lifting body is generally capable of atmospheric reentry and unpowered glide [1]. Therefore, aerodynamic shape plays a crucial role in determining its performance, influencing thermal protection, flight trajectory, stability, maneuverability, aerodynamic capabilities, and structure. The lift-to-drag ratio (L/D) has a particularly important influence on flight performance, so a large L/D is a design objective. During gliding, the windward side of the lifting body has the largest contact area with the incoming flow, providing nearly all of the lift force, so it is the key component that affects aerodynamic performance [2]. To make the lifting body with a large L/D, this paper will optimize the aerodynamic performance of the windward side.

The associate editor coordinating the review of this manuscript and approving it for publication was Kai Li.

The parametric modeling method plays a crucial role in the aerodynamic shape design of a lifting body [3], influencing all aspects of the performance, particularly the L/D. Contrasting to traditional vehicles, the unique geometric characteristics of a lifting body require the parametric modeling method to provide adequate design space in the initial design stage, and high flexibility in the iterative design stage. Moreover, during the optimization process, the parametric model coupled with mesh deformation can improve the design efficiency, and the simple shape parameters can further minimize design variables.

There are many researches on parametric modeling of a lifting body. The common modeling methods include the B-spline method, non-uniform rational B-spline (NURBS) method, class/shape function transformation (CST) method, and free form deformation (FFD) technique [4]. Among these methods, the CST method has some advantages in wide

design space and smooth curve fitting, but it only works out better on simple curves of smooth connection [5], and the parameters are sensitive to global curves, so it is not flexibility enough to iterative design. By contrast, the FFD technique can be used in arbitrary geometrical models and it also can create random theoretical deformation results, thereby the FFD technique will provide a wide design space. Most importantly, the FFD technique can create new shapes globally or locally and more details can be expressed. In addition, the FFD technique can be coupled with mesh deformation [6], [7], so it is highly suitable for parametric modeling of the lifting body shape.

Current research on the free form deformation (FFD) technique is mostly focused on traditional aircrafts mechanisms such as airfoils and wings, while few studies have considered advanced lifting body shapes. In this work, an example using the shape of an HTV-2 is used to introduce the FFD technique. Analysis of the characteristics of common FFD techniques is then conducted, including the Bernstein-based FFD technique [8], B-spline-based FFD (BFFD) technique [9], and NURBS-based FFD (NFFD) technique [10]. The results acquired in this study provide a guide for future FFD modeling of the lifting body.

A conflict exists between accuracy and efficiency when predicting aerodynamic performance in ASO problems, especially in a multiple iterative process. High fidelity computational fluid dynamics (CFD) such as Reynolds-averaged Navier-Stokes (RANS) equations have been commonly employed, however, they have high computational requirements. With hundreds or thousands of iterations in ASO works, the high amount of numerical results and time required is impractical. In order to minimize computation, a number of engineering estimation methods have also been widely used in ASO [11], such as the Newtonian method, Dahlem-Buck method, and Prandtl–Meyer method. With hypersonic speed and high altitude, the viscosity effect has a significant influence on the aerodynamic performance of a lifting body. The present challenge is that engineering estimation method is high efficiency but low fidelity with non-viscous, while credible CFD methods are accurate but time-consuming. Therefore, an efficient aerodynamic simulation method must be developed to produce a credible result with minimum computational requirements.

Using surrogate-based optimization is another effective strategy to reduce costs [12]. The main concept of surrogate-based optimization is to construct a highly functioning surrogate model to replace time-consuming CFD simulation [13]. Several popular surrogate models including polynomials, radial basis functions, kriging, and support vector regression can be used in surrogate-based optimization. Among these, the kriging model [14] has advantages in approximating nonlinear and multi-modal functions used for the ASO of vehicles. The surrogate models are first trained by initial sample points, which can be generated by experiments such as the design explorer orthogonal array (DEOA) method and Latin hypercube sampling (LHS) method. During the optimization process, the surrogate models are updated by an infill criterion at every step. Commonly used infill criterions include the expected improvement (EI) criterion [15], probability of improvement (PI) criterion, and lower confidence bounding (LCB) criterion. Using surrogate-based optimization methods can significantly improve design efficiency without much loss of accuracy.

TABLE 1. Shape parameters of the typical hypersonic lifting body.

shape parameters	L_1	L_2	W	H_1
values	3m	1m	1m	0.42m
shape parameters	H_2	r	θ_1	θ_2
values	0.18m	0.01m	16°	5.7°

Considering the challenges detailed above, an effective ASO method for a hypersonic lifting body is developed in this paper, consisting of a feasible FFD technique, an efficient aerodynamic simulation method, and a surrogate-based optimization method.

This paper is organized as follows. The next section introduces the FFD technique for a typical hypersonic lifting body. In Section 3, we analyze three FFD techniques by modeling of a line and a windward side with different basis functions. In Section 4, we introduce an efficient aerodynamic simulation method and surrogate-based optimization method. Section 5 describes the optimization problem of a constrained aerodynamic shape of a lifting body based on NFFD technique. Then, we validate and discuss this approach in an L/D maximization case of a lifting body in Section 6. Section 7 completes the paper with the conclusion.

The novelty of this paper is the first time the FFD technique is applied in the local model of a hypersonic lifting body, and an efficient aerodynamic shape design method is developed by the NFFD technique, the efficient aerodynamic simulation method and the surrogate-based optimization method.

II. FFD TECHNIQUE FOR LIFTING BODY

The FFD is a universal parametric modeling technique which is widely used in ASO for aircrafts. In this section, the FFD-based parametric modeling for hypersonic lifting body is discussed and some commonly used basis functions are introduced.

A. GEOMETRIC MODEL

To specify the FFD technique, a typical hypersonic lifting body mimicking the aerodynamic shape of HTV-2 is used as an example, as shown in Fig. 1. Due to the constraint of the thermal environment, the leading edge has been blunted with radius $r = 10$ mm. The main shape parameters of the typical hypersonic lifting body model are provided in Table 1.

The typical lifting body vehicle has a total length of 4.0 m, a total width of 2.0 m, and a total height of 0.6 m. As previously mentioned, the windward side provides nearly all the lift force and exerts the most influence on the aerodynamic performance of the lifting body vehicle. Thus, the ASO of the windward side is the focus of this paper.

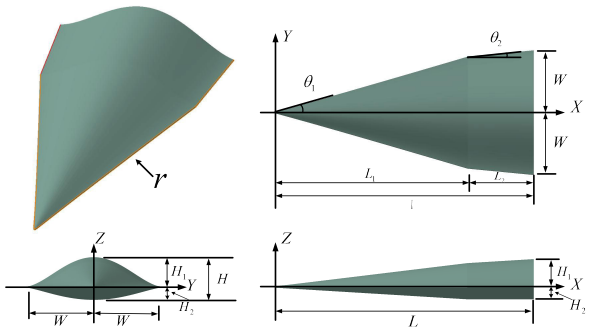

FIGURE 1. Geometric model of a typical hypersonic lifting body.

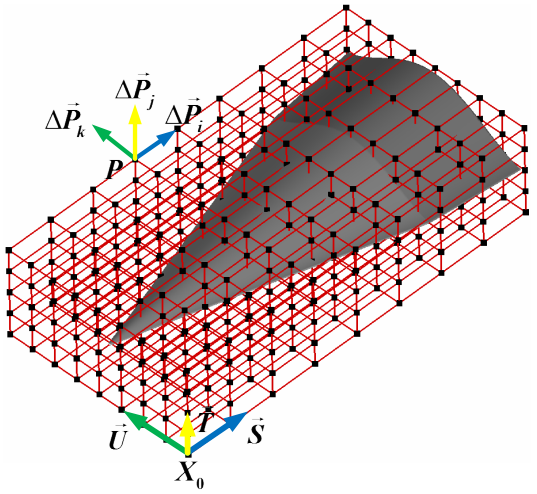

FIGURE 2. The control lattice and local coordinate system.

B. DEFINITION

The FFD method takes an elastic control lattice to contain the to-be-deformed lifting body vehicle, and creates a suitable mapping relation between the geometric mesh points and control points. The shape of lifting body vehicle will be deformed together with the movement of control points.

The parallel hexahedral control lattice is commonly used during the FFD modeling, and it should contain the lifting body vehicle, as shown in Fig. 2. The control lattice consist of red control points and black wireframe.

The FFD is defined in the local coordinate system X_0-STU of a unit cube, so we should transfer the coordinates (x, y, z) to local coordinates (s, t, u).

$$\vec{X} = \vec{X}_0 + s\vec{S} + t\vec{T} + u\vec{U} \tag{1}$$

where s, t, u $(0 \le s, t, u \le 1)$ are the local coordinates of $\vec{X}$.

The control points $\vec{P}_{i,j,k}$ are located on the control lattice, and the number of control points along the axial vectors of $\vec{S}$, $\vec{T}$, and $\vec{U}$ are $(l+1)$, $(m+1)$, and $(n+1)$ respectively. Any control point $\vec{P}_{i,j,k}$ can be defined as

$$\vec{P}_{i,j,k} = \vec{X}_0 + \frac{i}{l}\vec{S} + \frac{j}{m}\vec{T} + \frac{k}{n}\vec{U} \tag{2}$$

where i, j, and k $(i = 0, 1, \cdots, l;\ j = 0, 1, \cdots, m;\ k = 0, 1, \cdots, n)$ are the sequences of the control points along the axial vectors of $\vec{S}$, $\vec{T}$, and $\vec{U}$.

The deformation of the geometric model is controlled by moving the control points $\vec{P}_{i,j,k}$, so the deformation mapping between the geometric mesh points and control points is key in FFD method. In particular, the deformation mapping is mainly based on the basis function $R(\cdot)$, and the deformation mapping between the mesh point $\vec{X}$ and the control point $\vec{P}_{i,j,k}$ is generally written as

$$\vec{X} = \sum_{i=0}^{l}\sum_{j=0}^{m}\sum_{k=0}^{n} R_i(s)R_j(t)R_k(u)\cdot\vec{P}_{i,j,k} \tag{3}$$

where $R_i(s)$, $R_j(t)$, and $R_k(u)$ are the basis functions along the axial vectors of $\vec{S}$, $\vec{T}$, and $\vec{U}$.

C. DIFFERENT BASIS FUNCTIONS

The basis function $R(\cdot)$ of the FFD method plays an important role in the deformation mapping. Commonly used basis functions include Bernstein polynomial, B-Spline function, and the NURBS function.

1) BERNSTEIN POLYNOMIAL

As mentioned in Eq. (3), the $R_i(s)$, $R_j(t)$ and $R_k(u)$ are basis functions of FFD method along different directions, which has similar expressions. Take the $R_i(s)$ along $\vec{S}$ direction as an example, the expression of basis function based on Bernstein polynomial is

$$R_i(s) = C_l^i s^i (1-s)^{l-i} = \frac{(l)!}{(i)!\,(l-i)!} s^i (1-s)^{l-i} \tag{4}$$

So the deformation mapping relation between control point $\vec{P}_{i,j,k}$ and mesh point $\vec{N}(x, y, z)$ can be demonstrated as

$$\vec{N}(x,y,z) = \sum_{i=0}^{l} C_l^i s^i (1-s)^{l-i} \left[\sum_{j=0}^{m} C_m^j t^j (1-t)^{m-j} \times \left[\sum_{k=0}^{n} C_n^k u^k (1-u)^{n-k}\cdot\vec{P}_{i,j,k}\right]\right] \tag{5}$$

where s, t, and u are local coordinates of the geometric mesh points, and i, j and k are sequences of the control points along $\vec{S}$, $\vec{T}$ and $\vec{U}$ directions. The number of control points are $(l+1)$, $(m+1)$, and $(n+1)$.

2) B-SPLINE FUNCTION

Take the B-spline function $B_{i,p}(s)$ as the basis function, the B-spline-based FFD method can be called as the BFFD method. The expression of $R_i(s)$ in BFFD method can be written as

$$R_i(s) = \frac{B_{i,p}(s)}{\sum_{a=0}^{l} B_{a,p}(s)} \begin{cases} B_{i,0}(s) = \begin{cases} 1, & s_i \le s \le s_{i+1} \\ 0, & others \end{cases} \\ B_{i,p}(s) = \dfrac{s - s_i}{s_{i+p} - s_i} B_{i,p-1}(s) \\ \quad + \dfrac{s_{i+p+1} - s}{s_{i+p+1} - s_{i+1}} B_{i+1,p-1}(s), \quad p \ge 2 \end{cases} \tag{6}$$

So the deformation mapping relation of BFFD method between control point $\vec{P}_{i,j,k}$ and mesh point $\vec{B}(x, y, z)$ can be demonstrated as

$$\vec{B}(x,y,z)=\sum_{i=0}^{l}\frac{B_{i,p}(s)}{\sum_{a=0}^{l}B_{a,p}(s)}\left(\sum_{j=0}^{m}\frac{B_{j,q}(t)}{\sum_{b=0}^{m}B_{b,q}(t)}\times\left(\sum_{k=0}^{n}\frac{B_{k,r}(u)}{\sum_{c=0}^{n}B_{c,r}(u)}\cdot\vec{P}_{i,j,k}\right)\right) \tag{7}$$

where s, t and u are local coordinate values of geometric mesh points, and i, j and k are sequences of the control points along $\vec{S}$, $\vec{T}$ and $\vec{U}$ directions. The number of control points are $(l+1)$, $(m+1)$, and $(n+1)$, the orders of B-spline basis function are p, q, and r.

3) NURBS FUNCTION

Taking the NURBS function $N_{i,p}(s)$ as the basis function, the NURBS-based FFD method can be referred to as the NFFD method. The $N_{i,p}(s)$ is a non-uniform rational $B_{i,p}(s)$, and it introduce the weight factor ω to control the deformation, so the expression of $R_i(s)$ in NFFD method can be expressed as

$$\begin{aligned}R_i(s)=&\frac{\omega_i N_{i,p}(s)}{\sum_{a=0}^{l}\omega_a N_{a,p}(s)}\\&\times\begin{cases}N_{i,0}(s)=\begin{cases}1, & s_i\le s\le s_{i+1}\\0, & others\end{cases}\\N_{i,p}(s)=\dfrac{s-s_i}{s_{i+p}-s_i}N_{i,p-1}(s)\\\quad+\dfrac{s_{i+p+1}-s}{s_{i+p+1}-s_{i+1}}N_{i+1,p-1}(s), \quad p\ge 2\end{cases}\end{aligned} \tag{8}$$

The deformation mapping relation of the NFFD method between control point $\vec{P}_{i,j,k}$ and mesh point $\vec{N}(x, y, z)$ can then be denoted as

$$\vec{N}(x,y,z)=\sum_{i=0}^{l}\frac{\omega_i N_{i,p}(s)}{\sum_{a=0}^{l}\omega_a N_{a,p}(s)}\left(\sum_{j=0}^{m}\frac{\omega_j N_{j,q}(t)}{\sum_{b=0}^{m}\omega_b N_{b,q}(t)}\times\left(\sum_{k=0}^{n}\frac{\omega_k N_{k,r}(u)}{\sum_{c=0}^{n}\omega_c N_{c,r}(u)}\cdot\vec{P}_{i,j,k}\right)\right) \tag{9}$$

where s, t, and u are local coordinate values of geometric mesh points, and i, j and k are sequences of the control points along $\vec{S}$, $\vec{T}$, and $\vec{U}$ directions. The number of control points are $(l+1)$, $(m+1)$, and $(n+1)$, the orders of the NURBS basis function are p, q, and r, and ω_i, ω_j, and ω_k are the weight factors of the design point.

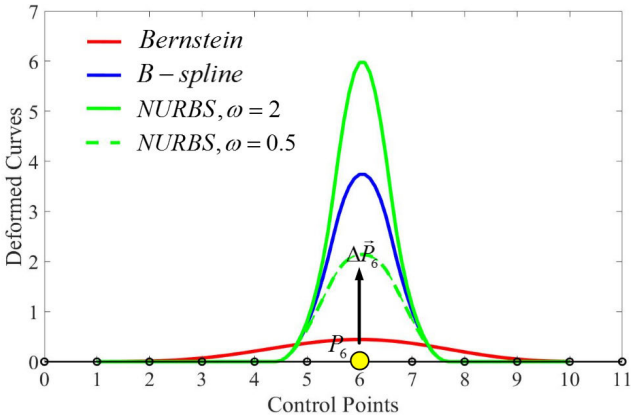

FIGURE 3. Deformed curves of a line based on different FFD techniques.

III. FFD MODELING ANALYSIS

Based on the above-mentioned FFD techniques with different basis functions, various mapping relations can be set between control points and mesh points, which means that different geometric deformations will be created under the same displacements of control points. To analyze the differences among the FFD techniques (original FFD technique, BFFD technique, and NFFD technique), the FFD modeling of a line and the windward side of a hypersonic lifting body are used as analytical examples.

A. FFD MODELING OF A LINE

As a simplified example, a line with an interval of [1, 10] is used to analyze the different deformed results among three FFD techniques, as shown in Fig. 3. The FFD control points $P_0 \sim P_{11}$ are evenly distributed at an interval of [0, 11].

Under the same displacement change of $\Delta\vec{P}_6 = 1.0$, the lines are deformed to various curves based on different FFD techniques. The basis function orders of the BFFD and NFFD techniques are all $r = 2$. The deformed curves are provided in Fig. 3, in which the red curve is created by the original FFD technique, the blue curve is created by the BFFD technique, the green solid curve is created by the NFFD technique with weight factor of $\omega = 2$, and the green dotted curve is created by the NFFD technique with weight factor of $\omega = 0.5$.

The deformed curves in Fig. 3 illustrate that all three FFD techniques have the same deformation tendency on the line, while their deformation range and degrees vary. Specifically, the original FFD technique causes global deformation with moderate deformation degree, as seen in the red curve in Fig. 3, while the BFFD and NFFD techniques focus on the local deformation with large deformation degree, as illustrated by the blue and green curves.

In addition, the weight factor ω of the NFFD technique gives the deformed curves more flexibility and wider deformation space [16] (when $\omega = 1$, it is the BFFD technique).

B. FFD MODELING OF THE WINDWARD SIDE

The FFD modeling of a line demonstrates the deformation differences visually. The windward side of a hypersonic

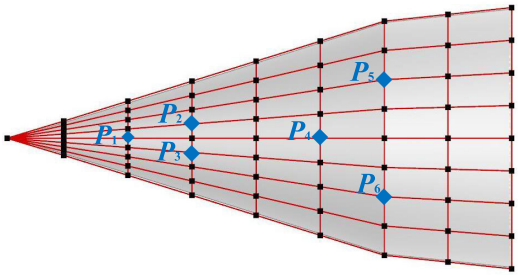

FIGURE 4. The irregular control lattice and distribution of design points.

TABLE 2. The sequences and displacements of the design points.

	P_1	P_2	P_3	P_4	P_5	P_6
i	4	5	3	4	6	2
j	0, 1	0, 1	0, 1	0, 1	0, 1	0, 1
k	6	5	5	3	2	2
$\Delta\vec{P}$	2	-4	-4	6	-8	-8

lifting body then used to conduct depth analysis. Taking the typical windward side in Fig. 1 as an example, we take a border-based FFD control surface [17] to replace the traditional FFD control lattice in this paper. The border-based FFD control surface takes the projected edge of the windward side as the boundary of the control lattice, as shown in Fig. 4. As an irregular control lattice, the border-based FFD control surface is geometrically consistent with the to-be-deformed windward side, so it can improve operational efficiency and geometric continuity [17].

The total number of control points is $9 \times 2 \times 9$ ($\vec{S} \times \vec{T} \times \vec{U}$), and six design points $P_1 \sim P_6$ are selected on the control lattice, as shown in Fig. 4. To simplify the deformation, the displacements of design points in the $\vec{Y}$ direction are manipulated. The sequence (i, j, k) in the local coordinate system of the design points $P_1 \sim P_6$ and their displacements $\Delta\vec{P}_1 \sim \Delta\vec{P}_6$ are listed in Table 2.

Under the same displacements of $\Delta\vec{P}_1 \sim \Delta\vec{P}_6$, the original FFD, BFFD, and NFFD techniques are adopted to create deformation on the windward side. The basis function orders of the BFFD and NFFD techniques are all $q = 2$, and deformation results of the windward side are provided in Fig. 5. To further analyze the deformation ranges and degrees on the windward side, the contours of the Y coordinate on the windward side under different FFD techniques are shown in Fig. 6.

Both Fig. 5 and Fig. 6 illustrate that under the same displacements of the design points $\Delta\vec{P}_1 \sim \Delta\vec{P}_6$, the deformation range and degrees on the windward side of three FFD techniques are different. The deformation of the original FFD technique is not obvious, and the BFFD and NFFD techniques focus on local deformation with a large deformation degree. Although the deformation tendencies of the BFFD and NFFD

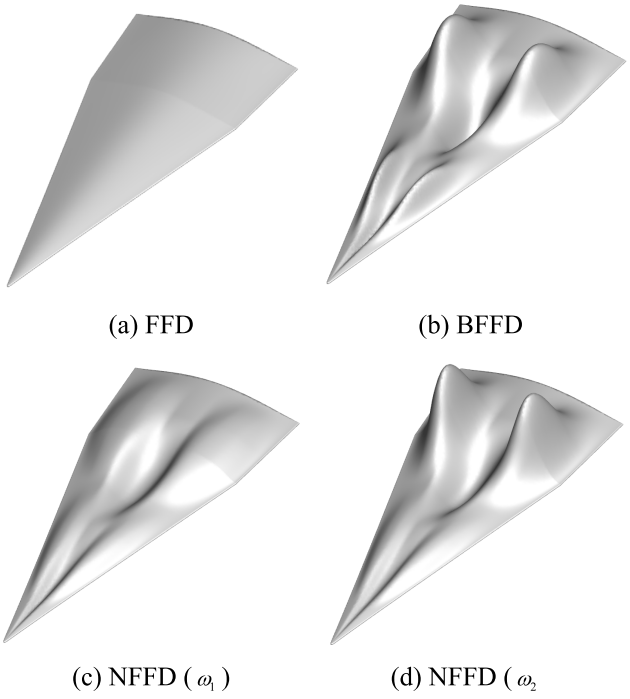

FIGURE 5. Deformation results of the windward side under the different FFD techniques: (a) Original FFD technique; (b) BFFD technique; (c) NFFD technique with weight factor $\omega_1 = (2, 5, 5, 3, 8, 8)$; (d) NFFD technique with weight factor $\omega_2 = (3, 5, 5, 2, 0.5, 0.5)$.

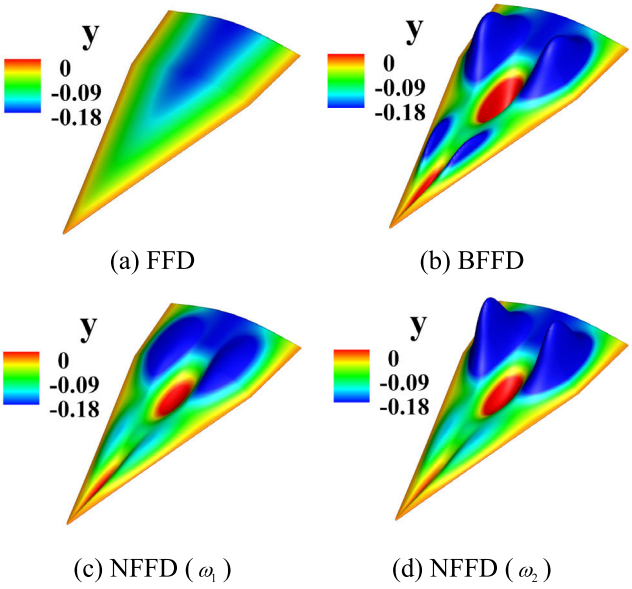

FIGURE 6. Contours of the Y coordinate on the windward side under different FFD techniques.

techniques are same, the weight factor ω equips the NFFD technique with wider deformation space.

By comparison, it is clear that the basis function $R(\cdot)$ plays an important role in deformation. Among three techniques, the NFFD technique not only includes the characteristics of the other FFD techniques, but also introduces an additional weight factor ω to enable a more flexible and wider

design space. Thus, it is more suitable for deformable modeling of the windward side.

IV. SIMULATION AND OPTIMIZATION METHODS

The aerodynamic design and optimization of the hypersonic lifting body can be further advanced by NFFD modeling of the windward side. To balance time cost and calculation accuracy, an efficient aerodynamic simulation method is adopted to calculate the aerodynamic force, and the surrogate-based optimization method is used to search the optimal solution. The simulation and optimization methods are introduced as follows.

A. EFFICIENT SIMULATION METHOD

The tradeoff between time cost and calculation accuracy is a persistent issue in aerodynamic design. The Euler plus friction drag method has been demonstrated to be the best technique through its use in the design of the hypersonic vehicle HIFiRE-4 [18]. In this paper, an efficient aerodynamic simulation method is introduced which combines Euler equations (non-viscous component) and skin friction drag (viscous component based on compressible turbulence model), and its accuracy is validated.

1) EFFICIENT AERODYNAMIC SIMULATION METHOD

Euler equations are first used to calculate the three-dimensional compressible and non-viscous aerodynamic force. When the incoming fluid is the perfect gas, the Euler equations can be written as:

$$\int_{\Omega} \frac{\partial \vec{Q}}{\partial t} dV + \int_{\partial\Omega} \left(\vec{F} \cdot \vec{n}\right) ds = 0 \tag{10}$$

where Ω is the control volume, t is the time, $\vec{Q}$ is the state vector which consists of flow variables, $\vec{F}$ is the flux vector, and $\vec{n}$ is a unit vector.

The skin friction coefficient C_f is then adopted to calculate the viscous aerodynamic force. For the compressible turbulence model, Schlichting [19] proposed a skin friction coefficient which can be written as:

$$C_f = \frac{0.02296}{Re^{*0.139}} \left(\frac{\rho^*}{\rho_e}\right)^{0.861} \left(\frac{\mu^*}{\mu_e}\right)^{0.139} \tag{11}$$

where C_f is the skin friction coefficient, Re^* is the reference Reynolds number, ρ^* is the reference density, μ^* is the reference viscosity coefficient, ρ_e is the density at the edge of the boundary layer, and μ_e is the viscosity at the edge of the boundary layer.

The reference enthalpy method [20] is used next to calculate the values of Re^*, ρ^* and μ^*. The most popular reference enthalpy method proposed by Eckert [21] and Meador and Smart [20] was developed directly from compressible boundary-layer equations solutions. The expression of the Meador's reference enthalpy method is:

$$\frac{H^*}{H_e} = 1 + 0.5\left(\frac{H_w}{H_e} - 1\right) + 0.16r\frac{\gamma - 1}{2} Ma_e^2 \tag{12}$$

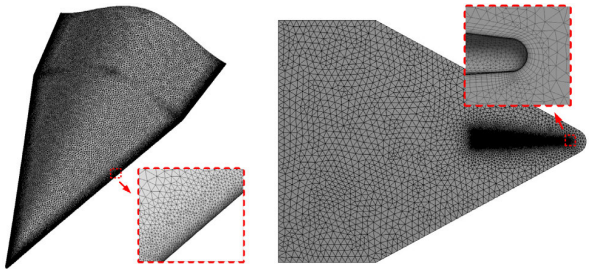

(a) Surface mesh (b) Volume mesh for RANS equations

FIGURE 7. Mesh of typical hypersonic lifting body.

where H^* is the reference enthalpy, H_w is the enthalpy on the wall, H_e is the enthalpy at the edge of the boundary layer, Ma_e is the Mach number at the edge of the boundary layer, r is the recovery factor that depends on the Prandtl number, and γ is the ratio of specific heats.

In this paper, the table-look-up method is used to obtain the reference values, and the Sutherland formula corrected by Keyes [22] is utilized to determine the reference viscosity coefficient:

$$\frac{\mu^*}{\mu_e} = \left(\frac{T^*}{T_e}\right)^{1.5} \left(\frac{T_e + 122.1 \times 10^{-\frac{5}{T_\infty}}}{T^* + 122.1 \times 10^{-\frac{5}{T'}}}\right) \tag{13}$$

where T^* is the reference temperature, and T_e is the temperature at the edge of the boundary layer.

2) VALIDATION

In this section, the efficient aerodynamic simulation method is used simulate the aerodynamic performance of a typical hypersonic lifting body. As an accurate reference, the CFD result is simulated by three-dimensional RANS equations [23] using the shear-stress transport ($SST\ k-\omega$) turbulence model. In the computation of the CFD process, the air is assumed to be perfect gas, and the viscosity coefficient is calculated by Sutherland law.

The surface mesh is created by the Delaunay method, and consists of 7.93×10^4 nodes and 1.58×10^5 triangular elements, as shown in Fig. 7(a). The volume mesh for an efficient aerodynamic simulation method is created by the adaptive Cartesian methods, and the number of total elements is 1.89×10^6. The volume mesh for RANS equations contains a boundary layer close to the surface mesh, and the number of total elements is 4.08×10^6, as shown in Fig. 7(b).

The computational states chosen in this paper include a flight height of 40 km, a Mach number of 8.0, and angles of attack of $-2°/0°/2°/5°/8°/10°$. Taking the results of RANS equations as the accurate reference, the calculation accuracy of the efficient aerodynamic simulation method proposed in this paper is validated. As the viscous effect mainly causes a difference in axial force coefficient Ca, and the L/D is the main factor to reflect the aerodynamic performance, comparison curves of Ca and L/D are provided in Fig. 8.

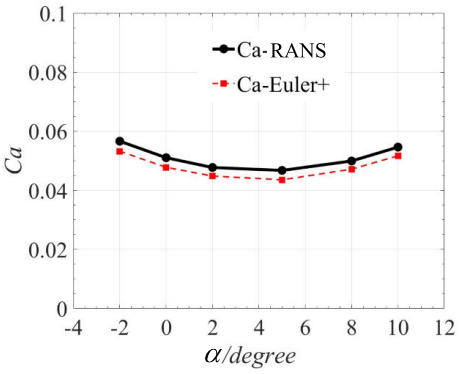

(a) *Ca*

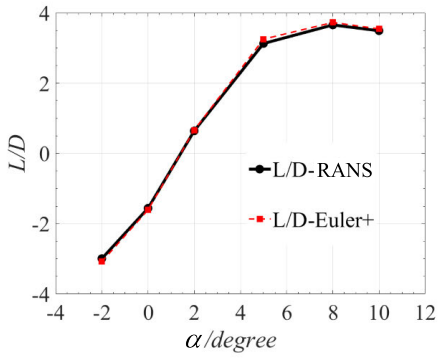

(b) *L/D*

FIGURE 8. Comparison of the aerodynamic results for RANS equations and efficient aerodynamic simulation method.

As illustrated in Fig. 8, the aerodynamic results of the efficient aerodynamic simulation method correspond reasonably well with the RANS equations, while the attack angle α varies from $-2°$ to $10°$. Although the *Ca* of the efficient aerodynamic simulation method are all less than the RANS equations, they exhibit the same variation tendency. More importantly, the characteristics of the L/D between the RANS equations and the efficient aerodynamic simulation method are in good accordance.

Detailed aerodynamic results of the concrete errors between the RANS equations and efficient aerodynamic simulation method are provided in Table 3. In addition, the *Error* is introduced to evaluate the relative errors between the results of efficient aerodynamic simulation method and the RANS equations, which can be written as

$$Error = \frac{Efficient^{+} - RANS}{RANS} \times 100\% \tag{14}$$

where *Error* is the relative error of the aerodynamic results, $Efficient^{+}$ is the aerodynamic results of the efficient aerodynamic simulation method, and *RANS* is the aerodynamic results of the RANS equations.

As Table 3 shows, the *Errors* of *Ca* are within 6.8% and the *Errors* of L/D are within 4% for all computational states, and the errors between the efficient aerodynamic simulation method and the RANS equations can be maintained stably for both *Ca* and L/D. The results confirm that the efficient aerodynamic simulation method can be accurately applied for evaluating aerodynamic performances within the specific design states.

In addition, the computation time of one design state required nearly 50 hours on 4 central processing units (CPUs) for the RANS equations, but only 0.5 hours on 1 CPU for the efficient aerodynamic simulation method. Compared with RANS, the efficient aerodynamic simulation method has higher efficiency.

B. SURROGATE-BASED OPTIMIZATION METHOD

To obtain the maximum improvement in the aerodynamic performance of the hypersonic lifting body, an infilling expected improvement (EI) criterion together with the multiobjective evolutionary algorithm based on decomposition (MOEA/D) method [24] is used in this paper. Besides, a kriging surrogate model is used to improve the optimization efficiency.

1) KRIGING SURROGATE MODEL

The kriging surrogate model has been widely used for aerodynamic design problems due to its accuracy and robustness [25]. In this study, the kriging surrogate model is constructed to reduce computational costs. Before building the surrogate model, there must be enough initial sample points to fill the design space. They are then calculated by the efficient aerodynamic simulation method proposed in this paper.

For an expensive function $y = f(\boldsymbol{x}), \boldsymbol{x} \in R^n$, the response values $\boldsymbol{Y}_s = \left\{y^1, \ldots, y^k\right\}^T$ (such as aerodynamic force coefficients *Cl* and *Cd* are respect to the k sample points $\boldsymbol{X} = \left\{\boldsymbol{x}^1, \ldots, \boldsymbol{x}^k\right\} \in R^n$ ($\boldsymbol{x}^i$ $(i = 1, \ldots, n)$ is n-dimensional vector). The kriging model assumes the response value and the variable subject to the Gaussian stochastic process, which defined as [12]

$$y = \mu + \varepsilon(\boldsymbol{x}) \tag{15}$$

where μ is the deterministic part, and $\varepsilon(\boldsymbol{x})$ is a Gaussian stochastic process.

Then based on the collected sample points $(\boldsymbol{X}, \boldsymbol{Y}_s)$, the best linear unbiased predictor of the predicted point is as follows

$$\hat{y}(\boldsymbol{x}) = \hat{\mu} + \boldsymbol{r}^T \boldsymbol{R}^{-1}\left(y - 1\hat{\mu}\right) \tag{16}$$

where $\hat{\mu} = \left(1^T \boldsymbol{R}^{-1} 1\right)^{-1} 1^T \boldsymbol{R}^{-1} Y_s$, $\boldsymbol{R}$ is a $k \times k$ correlation matrix whose (i, j)-element is $\boldsymbol{c}\left(\boldsymbol{x}^i, \boldsymbol{x}^j\right)$, and $\boldsymbol{r} = \left[\boldsymbol{c}\left(\boldsymbol{x}, \boldsymbol{x}^1\right), \ldots, \boldsymbol{c}\left(\boldsymbol{x}, \boldsymbol{x}^K\right)\right]^T$ The $\boldsymbol{c}\left(\boldsymbol{x}^i, \boldsymbol{x}^j\right)$ is the correlation function that depends on the distance between two points $\left(\boldsymbol{x}^i, \boldsymbol{x}^j\right)$, and the Gaussian function is used in this paper.

The kriging model can also give the mean squared error of the estimated value, and that is

$$s^2(\boldsymbol{x}) = \hat{\sigma}^2\left[1 + \frac{\left(1 - 1^T \boldsymbol{R}^{-1} r\right)^2}{1^T \boldsymbol{R}^{-1} 1} - r^T \boldsymbol{R}^{-1} r\right] \tag{17}$$

where $\hat{\sigma}^2 = \frac{(Y_s - 1\hat{\mu})^T \boldsymbol{R}^{-1} (Y_s - 1\hat{\mu})}{k}$.

TABLE 3. Results of RANS equations and efficient aerodynamic simulation method.

α/°	H=40 km, Ma=8.0					
	Ca			L/D		
	RANS	Efficient+	Error	RANS	Efficient+	Error
-2	5.66×10^{-2}	5.32×10^{-2}	-5.98%	-2.99	-3.08	2.83%
0	5.10×10^{-2}	4.53×10^{-2}	-6.37%	-1.56	-1.61	3.05%
2	4.77×10^{-2}	4.45×10^{-2}	-6.06%	0.64	0.66	3.58%
5	4.67×10^{-2}	4.36×10^{-2}	-6.80%	3.13	3.25	3.98%
8	4.99×10^{-2}	4.72×10^{-2}	-5.54%	3.66	3.73	1.97%
10	5.46×10^{-2}	4.84×10^{-2}	-5.41%	3.49	3.54	1.48%

The kriging surrogate model $N\left(\hat{y}\left(\boldsymbol{x}\right), s^2\left(\boldsymbol{x}\right)\right)$ can give the response value y^i at x^i for $i = 1, \ldots, k$, which can be regarded as a predictive distribution for the time-consuming CFD simulation.

2) INFILLING CRITERION

After constructing the kriging surrogate model based on initial sample points, the new sample points should be added to update the model, which will improve the predictive accuracy and approximate the optimal solution. During each cycle in the iterative optimization, a current optimal solution is calculated by the CFD method and added to the sample points, cycle by cycle, until the optimum is obtained.

Currently, the most popular infilling criteria is the expected improvement (EI) in the efficient global optimization (EGO) method [12]. This method is most likely to obtain the global optimal solution of the EI criteria, and has been widely used in aircraft design. Based on above kriging surrogate model $N\left(\hat{y}\left(\boldsymbol{x}\right), s^2\left(\boldsymbol{x}\right)\right)$, the expected improvement is

$$E\left[I\left(\boldsymbol{x}\right)\right] = \begin{cases} \left[\left(y_{\min} - \hat{y}\left(\boldsymbol{x}\right)\right)\right]\Phi\left(\dfrac{y_{\min} - \hat{y}}{\hat{s}\left(\boldsymbol{x}\right)}\right) \\ \quad + \hat{s}\left(\boldsymbol{x}\right)\phi\left(\dfrac{y_{\min} - \hat{y}}{\hat{s}\left(\boldsymbol{x}\right)}\right) & \hat{s} > 0 \\ 0 & \hat{s} = 0 \end{cases} \quad (18)$$

where $y_{\min}$ is the minimal value of all evaluated points.

A well compromise of exploration and exploitation [26] is the mainly advantage of the EI criteria. In detail, the term $\left[\left(y_{\min} - \hat{y}\left(\boldsymbol{x}\right)\right)\right]\Phi\left(\frac{y_{\min}-\hat{y}}{\hat{s}(\boldsymbol{x})}\right)$ in Equation (17) reflects the local search with less uncertainty, and the term $\hat{s}\left(\boldsymbol{x}\right)\phi\left(\frac{y_{\min}-\hat{y}}{\hat{s}(\boldsymbol{x})}\right)$ reflects the global search with much uncertainty.

Then compromising the global and local search, we define a two objective optimization problem by maximizing the expected improvement, and it is defined as

$$\max F = \left(\left[\left(y_{\min} - \hat{y}\left(\boldsymbol{x}\right)\right)\right]\Phi\left(\frac{y_{\min} - \hat{y}}{\hat{s}\left(\boldsymbol{x}\right)}\right) + \hat{s}\left(\boldsymbol{x}\right)\phi\left(\frac{y_{\min} - \hat{y}}{\hat{s}\left(\boldsymbol{x}\right)}\right)\right)^T, \quad \boldsymbol{x} \in \Omega \quad (19)$$

The main goal of this optimization problem is to tend to find a point that its predicted value smaller that $y_{\min}$ and/or there is much uncertainty associated with the prediction. But the global search and local search are usually conflicting, so the multi-objective optimization algorithm is needed to solve the MOP. In this study, the multiobjective evolutionary algorithm based on decomposition (MOEA/D) method [24] is employed for solving the MOP, which performs much better than other multiobjective evolutionary algorithms. The main idea is to decompose the MOP into some single objective subproblems and then optimizes them in a collaborative way.

V. LIFTING BODY SHAPE OPTIMIZATION

A. OPTIMIZATION PROBLEM

The typical hypersonic lifting body shown in Fig. 1 was chosen as the baseline and its geometry parameters are listed in Table 1. Designing a hypersonic lifting body is systematic, with most of the flight performances directly related to the *L/D,* including aerodynamic capabilities, trajectory, range, and maneuverability. In this section, the L/D was selected as the optimization objective.

The aerodynamic performance of the baseline was analyzed with the flight height of 40 km, Mach number of 8.0, and an angle of attack of 8° as the design point, which has a maximum $L/D = 3.73$, as shown in Table 3. Adequate volume for inner loading requirements is also important for the design of a factual hypersonic lifting body [27]. As a design constraint, the volume of inner loading $V_{loading}$ is added into the optimization problem, as shown in Fig. 9. Without loss of generality, a loading of frustum (yellow in color) was set inside the lifting body, with geometric parameters of $l = 2000mm$, $h_1 = 175mm$, and $h_2 = 450mm$. During optimization, the lower limit of $V_{loading}$ corresponds to the value of baseline $V_{loading\_base}$, so the volume constraint of inner loading is $V_{loading} \geq V_{loading\_base}$.

In this case, aerodynamic results such as lift force, drag force, and L/D, can be calculated by the efficient aerodynamic simulation method, which has been validated with credible accuracy and high efficiency. Based on the surrogate-based optimization method, the maximum L/D of the typical hypersonic lifting body is obtained by manipulating its shape

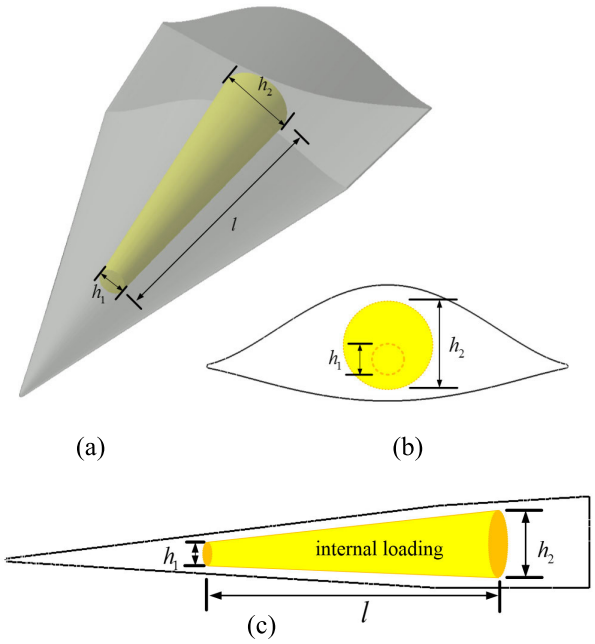

FIGURE 9. Inner loading of the typical hypersonic lifting body.

TABLE 4. Description of ASO problem.

Optimization problem	Description
Design point	$H = 40km,\ Ma = 8,\ \alpha = 8^{\circ}$
Objective function	$\max(L/D)$
Constraint	$V_{loading} \geq V_{loading\_base}$
Design variables	NFFD design control points
Simulation method	Efficient aerodynamic simulation method
Optimization method	Surrogate-based optimization method

using the NFFD technique, while satisfying the volume constraint of inner loading $V_{loading} \geq V_{loading\_base}$.

The description of the ASO problem of the hypersonic lifting body is listed in Table 4.

B. NFFD MODELING

During NFFD modeling, an irregular control lattice of $30 \times 2 \times 20$ ($\vec{S} \times \vec{T} \times \vec{U}$) is used to parameterize the typical hypersonic lifting body, and various design points are within the yellow zone, as shown in Fig. 10. The sequences (i, k) of the design points along $\vec{S}$ and $\vec{U}$ directions are presented near the control lattice, and the design points along $\vec{T}$ direction are overlapped with sequences $j = 0, 1$.

During optimization, the order of NURBS basis function is chosen as $q = 8$ to achieve fairing deformation. In order to simplify the optimization problem, only the Y coordinates of the design points can be manipulated.

To reduce the design space, all the design points consist of six design variables $X_1 \sim X_6$. The sequences (i, j, k) of the design points on NFFD lattice are shown in Table 5. Because a volume constraint was included for inner loading, there are

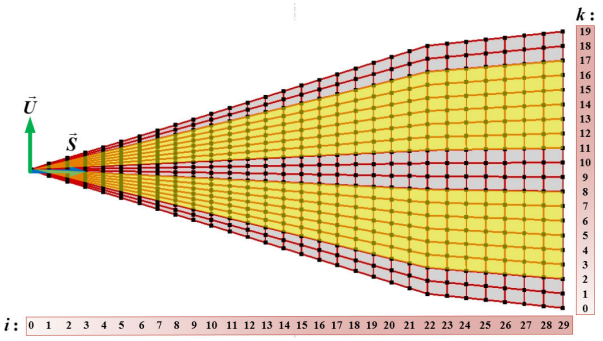

FIGURE 10. Irregular control lattice and control points.

no design points with sequences $k = 9, 10$, resulting in no deformation in the middle of the windward side.

C. OPTIMIZATION CONDITION

Before the optimization operation, an initial sample of 65 is generated by the LHS method. The lower/upper bounds and design ranges of the design variables $X_1 \sim X_6$ are shown in Table 6.

With the initial surrogate model, infilling EI criterion is applied to add new samples and predict the optimal result. During the surrogate-based optimization, the Gauss function is taken as the correlation function, and the maximum number of optimization iterations is 70. The conditions of the optimization problem are listed in Table 7.

The process of the ASO based on NFFD modeling is illustrated by the flowchart in Fig. 11. The detailed process of NFFD modeling is described in the blue dotted box. By integrating the efficient aerodynamic simulation method and the surrogate-based optimization method proposed in this paper, the optimal shape of the lifting body can be determined.

VI. RESULTS AND DISCUSSION

The constrained aerodynamic shape of the lifting body is optimized based on the flowchart in Fig. 11. Next, 65 (refer to $11n$-1, n is the number of design variables) initial samples are generated in the six-dimensional space and the aerodynamic shape is optimized on 60 optimization iterations, which contain a total of 125 steps.

As illustrated in Fig. 12, the convergent result of the maximum L/D versus process step is reasonable. After establishing the sampling model, the L/D increases sharply when optimization begins, then gradually increases until the convergence of $\max\ (L/D)_{Optimal} = 4.31$ at $step = 102$.

Detailed data of the design variables $X_1 \sim X_6$ and the maximum L/D during optimization is also provided in Table 8. It can be observed that all design variables are positive, and many design variables have reached or are approaching the upper bounds. At this point, the volume constraint of the inner loading restricts further improvement of aerodynamic performance.

Figure 13 provides a comparison of the geometric models between the base shape and the optimal shape, and

TABLE 5. Sequences of the design points on NFFD lattice (j = 0, 1).

k \ i	0~3	4	5	6	7,8	9,10	11,12	13,14
0,1,9,10,18,19	0	0	0	0	0	0	0	0
2,17	0	$X_1/32$	$X_1/16$	$X_1/8$	$X_1/4$	$(X_1+X_2)/8$	$X_2/4$	$(X_2+X_3)/8$
3,16	0	$X_1/16$	$X_1/8$	$X_1/4$	$X_1/2$	$(X_1+X_2)/4$	$X_2/2$	$(X_2+X_3)/4$
4~7,12~15	0	$X_1/8$	$X_1/4$	$X_1/2$	X_1	$(X_1+X_2)/2$	X_2	$(X_2+X_3)/2$
8,11	0	$X_1/24$	$X_1/14$	$X_1/6$	$X_1/3$	$(X_1+X_2)/6$	$X_2/3$	$(X_2+X_3)/6$

k \ i	15,16	17,18	19,20	21,22	23,24	25,26	27~29
0,1,9,10,18,19	0	0	0	0	0	0	0
2,17	$X_3/4$	$(X_3+X_4)/8$	$X_4/4$	$(X_4+X_5)/8$	$X_5/4$	$(X_5+X_6)/8$	$X_6/4$
3,16	$X_1/24$	$X_1/14$	$X_1/6$	$X_1/3$	$(X_1+X_2)/6$	$X_2/3$	$(X_2+X_3)/6$
4~7,12~15	X_3	$(X_3+X_4)/2$	X_4	$(X_4+X_5)/2$	X_5	$(X_5+X_6)/2$	X_6
8,11	$X_3/3$	$(X_3+X_4)/6$	$X_4/3$	$(X_4+X_5)/6$	$X_5/3$	$(X_5+X_6)/6$	$X_6/3$

TABLE 6. Lower/upper bounds and design ranges of the design variables.

	X_1	X_2	X_3	X_4	X_5	X_6
Lower bound	-0.3	-0.4	-0.6	-0.6	-0.6	-0.6
Upper bound	0.6	1.2	1.4	1.8	1.8	1.8
Design range	0.9	1.6	2.0	2.4	2.4	2.4

TABLE 7. Optimization condition of the ASO problem.

Optimization condition	Description
Design point	$H=40km,\ Ma=8,\ \alpha=8^{\circ}$
Objective function	max(*L*/*D*)
Constraint	$V_{loading} \geq V_{loading\_base}$
Design variables	NFFD design control points
Design Experiments	LHS method
Samples size	65
Kernel function	Gauss function
Infilling criterion	EI criterion
Optimization iteration	60

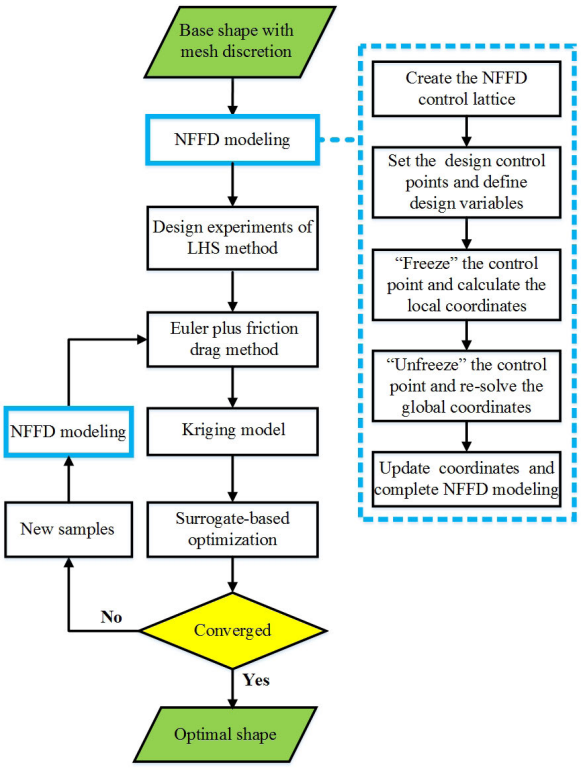

FIGURE 11. Flowchart of the ASO based on NFFD modeling.

Fig. 14 shows the comparison of the *Y* coordinate contour on the windward side. As illustrated in the figures, both sides of the optimal windward side significantly cave inward of the lifting body, especially in red zones of the *Y* coordinate contours.

As illustrated in Fig. 15, a typical section shows that the optimal shape still satisfies the inner loading constraint. If the inner loading constraint is not added in this case, the entire windward side would be caved in toward the body.

Table 9 shows the comparison of aerodynamic performance between the base shape and the optimal shape for the axial force coefficient *Ca*, normal force coefficient *Cn*, lift force coefficient *Cl*, drag force coefficient *Cd*, and the *L*/*D*. In addition, *Delta* is introduced to evaluate the relative changes between the base shape and the optimal shape, which can be written as

$$Delta = \frac{Optimization - Base}{Base} \times 100\% \tag{20}$$

where *Delta* is the relative change of the aerodynamic performances, *Optimization* is the aerodynamic results of the optimal shape, and *Base* is the aerodynamic performances of the base shape.

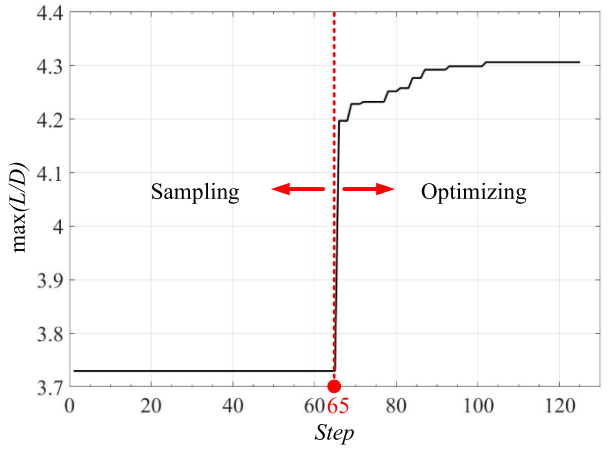

FIGURE 12. Convergent result of the maximum L/D versus step.

TABLE 8. Design variables $X_1 \sim X_6$ and the maximum *L/D* during optimization.

Step	L/D	X_1	X_2	X_3	X_4	X_5	X_6
base	3.73	0	0	0	0	0	0
66	4.20	0.40	0.23	0.56	1.33	1.45	1.8
69	4.22	0.28	0.39	0.66	1.26	1.29	1.47
72	4.23	0.32	0.37	0.75	1.32	1.33	1.51
78	4.25	0.31	0.45	0.79	1.32	1.38	1.60
81	4.26	0.16	0.50	0.82	1.28	1.38	1.60
84	4.28	0.09	0.39	0.72	1.31	1.56	1.72
87	4.29	0.06	0.37	0.89	1.44	1.66	1.77
93	4.30	0.05	0.42	0.90	1.57	1.66	1.79
102	4.31	0.14	0.49	0.94	1.56	1.69	1.80

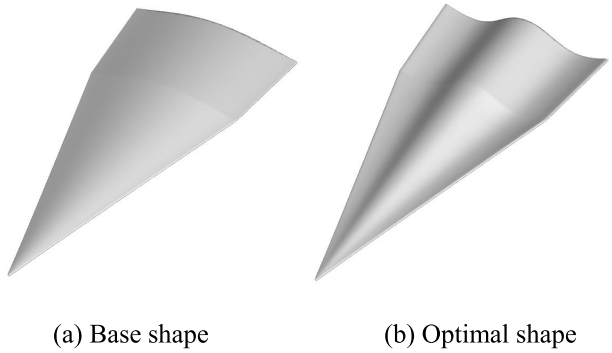

FIGURE 13. Comparison of the geometric model.

As observed in Table 9, all aerodynamic forces are reduced by optimization, and the reduced range of the *Cd* is larger than the *Cl*, meaning the L/D has been increased with the $Delta = 15.47\%$. To further observe the aerodynamic differences between the base and optimal shape, Fig. 16 shows a comparison of the pressure contour on the windward side.

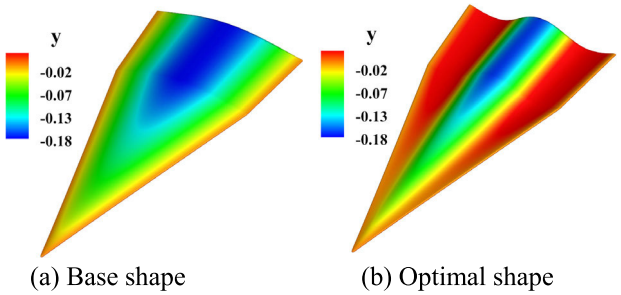

FIGURE 14. Comparison of the Y coordinate contour on the windward side.

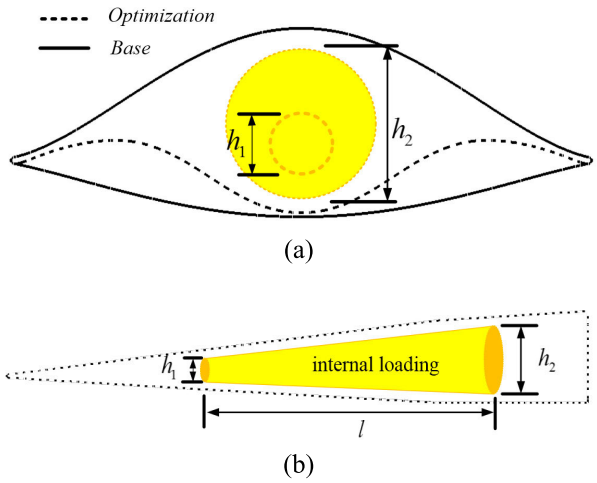

FIGURE 15. Comparison of the inner loading at a typical section.

TABLE 9. Comparison of aerodynamic performances.

	Ca	*Cn*	*Cl*	*Cd*	*L/D*
Base	4.71×10^{-2}	0.38	0.37	9.99×10^{-2}	3.73
Optimization	2.51×10^{-2}	0.28	0.28	6.41×10^{-2}	4.31
Delta/%	-46.76	-26.26	-25.9	-35.83	15.47

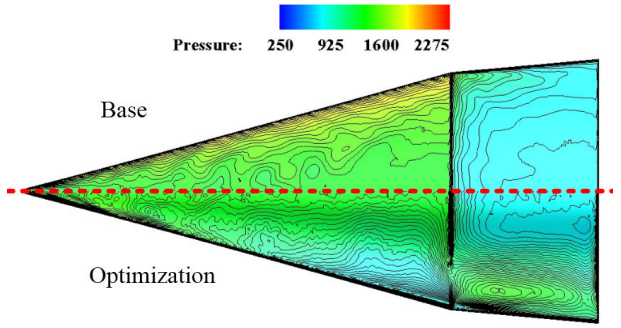

FIGURE 16. Comparison of the pressure contour on the windward side.

By comparison, the windward pressure of the optimal shape is generally smoother than that of the base shape. In detail, the pressure on the posterior segment of the optimal shape is larger than the base shape, and the pressure near the leading edge is smaller.

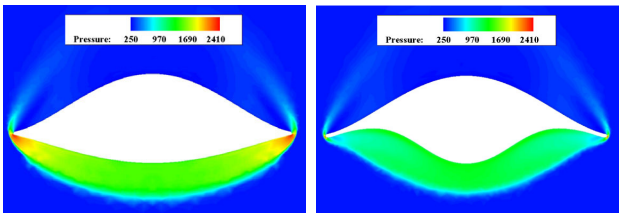

(a) Base shape (b) Optimal shape

FIGURE 17. Comparison of the pressure contour on a typical section.

A comparison of the pressure contour on a typical section ($x = 3.0$ m) is provided in Fig. 17. It is apparent that the pressure distribution on the leeward sides of the two shapes are similar, but on the windward side, the shock waves are obviously reduced from the base shape to the optimal shape, resulting in a drag reduction. By comparison, the windward pressure distribution of base shape is centralized on both edges, but the optimal shape has a nearly uniform pressure distribution.

To summarize, the optimal shape has a larger L/D than the base shape with $Delta = 15.47\%$, while satisfying the inner loading constraint. All results illustrate that the proposed model is both efficient and effective, providing a design method that is helpful to ASO of the hypersonic lifting body.

VII. CONCLUSION

An effective method for applying FFD technique in ASO of a hypersonic lifting body was presented in this paper. The commonly used FFD techniques of BFFD, NFFD, and the original FFD technique were analyzed, and NFFD-based parametric modeling of the lifting body was carried out. The NFFD technique not only allows for a wide design space, but also introduces a weight factor ω to provide a more flexible modeling of the windward side.

An efficient aerodynamic simulation method combining Euler equations (non-viscous component) and skin friction drag (viscous component based on the compressible turbulence model) was developed, and its accuracy validated. Within the specific design states, the errors of L/D were within 4% between the efficient aerodynamic simulation method and the RANS equations, but the time cost of the efficient aerodynamic simulation method was less than 1% of that for RANS equations. A kriging surrogate model combined with infilling EI criterion was then applied to conduct a surrogate-based optimization method.

Using six design variables, the maximum L/D of a base lifting body was obtained by manipulating its shape using the NFFD technique. With initial samples generated by the LHD method, an optimal shape with $(L/D)_{Optimal} = 4.31$ was achieved when the optimization converged. The optimal shape had a larger L/D than base shape with $Delta = 15.47\%$, while satisfying the inner loading constraint.

The principal goal of this study was to provide an efficient ASO of the hypersonic lifting body based on FFD Technique. While the optimization procedures are successful, the NFFD technique can enlarge the design space and obtain more feasible solutions. In addition, the efficient aerodynamic simulation method and surrogate-based optimization method provide a more effective design solution. Subsequent work will focus on developing a more advanced parametric modeling technique and investigating related research of simulation and optimization methods for hypersonic vehicles.

ACKNOWLEDGMENT

The authors would like to thank the reviewers and editors for their very constructive comments, which have helped to improve the quality of this paper.

REFERENCES

[1] Z. Li, C. Hu, C. Ding, G. Liu, and B. He, "Stochastic gradient particle swarm optimization based entry trajectory rapid planning for hypersonic glide vehicles," *Aerosp. Sci. Technol.*, vol. 76, pp. 176–186, May 2018.

[2] K. H. Javaid and V. C. Serghides, "Airframe-propulsion integration methodology for waverider-derived hypersonic cruise aircraft design concepts," presented at the 42nd AIAA Aerosp. Sci. Meeting Exhibit, Reno, NV, USA, 2004.

[3] D. A. Masters, N. J. Taylor, T. Rendall, C. B. Allen, and D. J. Poole, "Review of aerofoil parameterisation methods for aerodynamic shape optimisation," presented at the 53rd AIAA Aerosp. Sci. Meeting, Kissimmee, FL, USA, 2015.

[4] G. Yang, A. Da Ronch, J. Drofelnik, and Z.-T. Xie, "Sensitivity assessment of optimal solution in aerodynamic design optimisation using SU2," *Aerosp. Sci. Technol.*, vol. 81, pp. 362–374, Oct. 2018.

[5] F. Yi, W. Tang, J.-X. Ren, Y.-W. Gui, and Z.-Y. Guo, "Parametric geometry representation method for hypersonic Vehicle configuration," *ACTA Aerodynamica Sinica*, vol. 30, no. 4, pp. 546–550, 2012.

[6] B. Zhang, Z. Feng, T. Yang, B. Xu, and X. Sun, "Integrated improvement of the elasticity-based mesh deformation method based on robust parameters and mesh quality," *Proc. Inst. Mech. Eng., G, J. Aerosp. Eng.*, vol. 233, pp. 3078–3095, Jul. 2018.

[7] J. Niu, J. Lei, and T. Lu, "Numerical research on the effect of variable droop leading-edge on oscillating NACA 0012 airfoil dynamic stall," *Aerosp. Sci. Technol.*, vol. 72, pp. 476–485, Jan. 2018.

[8] T. W. Sederberg and S. R. Parry, "Free-form deformation of solid geometric models," *ACM SIGGRAPH Comput. Graph.*, vol. 20, no. 4, pp. 151–160, 1986.

[9] J. Griessmair and W. Purgathofer, "Deformation of solids with trivariate B-splines," in *Proc. Eurographics*, vol. 21, 1989, pp. 137–148.

[10] H. J. Lamousin and N. N. Waggenspack, "NURBS-based free-form deformations," *IEEE Comput. Graph. Appl.*, vol. 14, no. 6, pp. 59–65, Nov. 1994.

[11] D. Sziroczak and H. Smith, "A review of design issues specific to hypersonic flight vehicles," *Prog. Aerosp. Sci.*, vol. 84, pp. 1–28, Jul. 2016.

[12] D. R. Jones, M. Schonlau, and W. J. Welch, "Efficient global optimization of expensive black-box functions," *J. Global Optim.*, vol. 13, no. 4, pp. 455–492, 1998.

[13] Z. H. Han, "Kriging surrogate model and its application to design optimization: A review of recent progress," *Acta Aeronautica Astronautica Sinica*, vol. 37, no. 11, pp. 3197–3225, 2014.

[14] Z. Feng, Q. Zhang, Q. Zhang, Q. Tang, T. Yang, and Y. Ma, "A multiobjective optimization based framework to balance the global exploration and local exploitation in expensive optimization," *J. Global Optim.*, vol. 61, no. 4, pp. 677–694, 2014.

[15] J. Mockus, V. Tiesis, and A. Zilinskas, "The application of Bayesian methods for seeking the extremum," in *Toward Global Optimization*, vol. 2, L. C. W. Dixon and G. P. Szego, Eds. Amsterdam, The Netherlands: Elsevier, 1978, pp. 117–129.

[16] L. Piegl, "On NURBS: A survey," *IEEE Comput. Graph. Appl.*, vol. 1, no. 1, pp. 55–71, Jan. 1991.

[17] B. Zhang, Z. Feng, B. Xu, and T. Yang, "Free form deformation method applied to modeling and design of hypersonic glide vehicles," *IEEE Access*, vol. 7, pp. 61400–61414, 2019.

[18] T. Smith, K. Bowcutt, J. Selmon, L. Miranda, B. Northrop, K. Lau, T. Silvester, R. Mairs, E. Unger, A. Paull, R. Paull, D. Dolvin, and H. Alesi, "HIFiRE 4: A low-cost aerodynamics, stability, and control hypersonic flight experiment," presented at the 17th AIAA Int. Space Planes Hypersonic Syst. Technol. Conf., San Francisco, CA, USA, 2011.
[19] H. Schlichting, *Boundary-Layer Theory*, 7th ed. New York, NY, USA: McGraw-Hill, 1979.
[20] W. E. Meador and M. K. Smart, "Reference enthalpy method developed from solutions of the boundary-layer equations," *AIAA J.*, vol. 43, no. 1, pp. 135–139, 2005.
[21] E. R. G. Eckert, "Engineering relations for heat transfer and friction in high-velocity laminar and turbulent boundary-layer flow over surfaces with constant pressure and temperature," *Trans. ASME*, vol. 78, no. 6, pp. 1273–1283, 1956.
[22] M. H. Bertram, "Hypersonic laminar viscous interaction effects on the aerodynamics of two-dimensional wedge and triangular planform wings," Nat. Aeronautic and Space Admin., Washington, DC, USA, Tech. Rep. NASA TND-35231996, Aug. 1966.
[23] A. Amrit, L. Leifsson, and S. Koziel, "Multi-fidelity aerodynamic design trade-off exploration using point-by-point Pareto set identification," *Aerosp. Sci. Technol.*, vol. 79, pp. 399–412, Aug. 2018.
[24] Q. Zhang and H. Li, "MOEA/D: A multiobjective evolutionary algorithm based on decomposition," *IEEE Trans. Evol. Comput.*, vol. 11, no. 6, pp. 712–731, Dec. 2007.
[25] J. Liu, W.-P. Song, Z.-H. Han, and Y. Zhang, "Efficient aerodynamic shape optimization of transonic wings using a parallel infilling strategy and surrogate models," *Struct. Multidisciplinary Optim.*, vol. 55, pp. 925–943, Mar. 2016.
[26] A. I. J. Forrester and A. J. Keane, "Recent advances in surrogate-based optimization," *Prog. Aerosp. Sci.*, vol. 45, pp. 50–79, Jan./Apr. 2009.
[27] Y. Ma, T. Yang, Z. Feng, and Q. Zhang, "Hypersonic lifting body aerodynamic shape optimization based on the multiobjective evolutionary algorithm based on decomposition," *Proc. Inst. Mech. Eng. G, J. Aerosp. Eng.*, vol. 229, no. 7, pp. 1246–1266, 2015.

BIN ZHANG was born in Binzhou, Shandong, China, in 1990. He received the B.S. degree in aerospace engineering and the M.S. degree in aeronautical and astronautical science and technology from the National University of Defense Technology, Changsha, China, in 2013 and 2016, respectively, where he is currently pursuing the Ph.D. degree in aeronautical and astronautical science and technology.

His research interests include aerodynamic shape design and optimization of flight vehicles.

ZHIWEI FENG was born in Linfen, Shanxi, China, in 1984. He received the B.S. degree in aerospace engineering, the M.S degree in aeronautical and astronautical science and technology, and the Ph.D. degree in mechanics from the National University of Defense Technology, Changsha, China, in 2006, 2008, and 2014, respectively.

Since 2014, he has been a Lecturer with the National University of Defense Technology. His research interests include aerodynamic design and multi-objective optimization of flight vehicles.

BOTING XU was born in Shangrao, Jiangxi, China, in 1992. She received the B.S. degree in aerospace engineering and the M.S. degree in aeronautical and astronautical science and technology from the National University of Defense Technology, Changsha, China, in 2013 and 2016, respectively, where she is currently pursuing the Ph.D. degree in aeronautical and astronautical science and technology.

Her research interests include dynamic simulation and control of flight vehicles.

TAO YANG was born in Changde, Hunan, China, in 1962. He received the B.S. and M.S. degrees in solid rocket engine technology from the National University of Defense Technology, Changsha, China, in 1983 and 1989, respectively, and the Ph.D. degree in ballistics from the Nanjing University of Science and Technology, Nanjing, China, in 1992.

From 1992 to 1994, he was a Lecturer with the National University of Defense Technology, where he was an Associate Professor, from 1994 to 2001, and has been a Professor, since 2001. His research interests include overall design and optimization of flight vehicles, and aerospace propulsion theory and engineering.